

Population and Coherence Dynamics in Large Conjugated Porphyrin Nanorings

Giovanni Bressan,¹ Michael Jirasek,² Harry L. Anderson,² Stephen R. Meech^{1,*} and Ismael A. Heisler^{3,*}

¹*School of Chemistry, Norwich Research Park, University of East Anglia, Norwich NR4 7TJ, United Kingdom*

²*Department of Chemistry, University of Oxford, Chemistry Research Laboratory, Oxford OX1 3TA, United Kingdom³*

³*Departamento de Física, Universidade Federal do Paraná, Caixa Postal 19044, 81531-990 Curitiba, Parana, Brazil*

Corresponding authors: s.meech@uea.ac.uk ; heisler@fisica.ufpr.br

Abstract

In photosynthesis nature exploits the distinctive electronic properties of chromophores arranged in supramolecular rings for efficient light harvesting. Among synthetic supramolecular cyclic structures, porphyrin nanorings have attracted considerable attention as they have a resemblance to naturally occurring light-harvesting structures but offer the ability to control ring size and the level of disorder. Here, broadband femtosecond transient absorption spectroscopy, with pump pulses in resonance with either the high or the low energy sides of the inhomogeneously broadened absorption spectrum, is used to study the population dynamics and ground and excited state vibrational coherence in large porphyrin nanorings. A series of fully conjugated, alkyne bridged, nanorings constituted of between ten and forty porphyrin units is studied. Pump-wavelength dependent fast spectral evolution is observed. A fast rise or decay of the stimulated emission are observed when large porphyrin nanorings are excited on, respectively, the high or low energy side of the absorption spectrum. Such dynamics are consistent with the hypothesis of a variation in transition dipole moment across the inhomogeneously broadened ground state ensemble. Oscillatory dynamics on the sub-ps time domain are observed in both pumping conditions. A combined analysis of the excitation wavelength-dependent transient spectra along with the amplitude and phase evolution of the oscillations allows assignment to vibrational wavepackets evolving on either ground or excited states electronic potential energy surfaces. Even though porphyrin nanorings support highly delocalized electronic wavefunctions, with coherence length spanning tens of chromophores, the measured vibrational coherences remain localised on the monomers. The main contributions to the beatings are assigned to two vibrational modes localised on the porphyrin cores: a Zn-N stretching mode and a skeletal methinic/pyrrolic C-C stretching and in-plane bending mode.

Introduction

Tetrapyrroles have been extensively employed as building blocks of supramolecular biomimetic structures and as model systems for energy transfer between coupled chromophores.^{1,2} Their photophysics have been investigated with both steady-state and ultrafast time-resolved spectroscopic techniques.^{3–8} Butadiyne-linked, Zn Porphyrin nanorings are synthetic conjugated supramolecular nanosystems with distinctive topologies, such as cyclic (nested) rigid or flexible structures,⁹ and have a rich energy level structure, which has been rationalised in terms of Hückel theory.^{10–12} Their electronic excitations display highly nonlocal character^{13–16} giving them a resemblance to naturally occurring, bacteriochlorophyll-based, systems such as B800 and B850 in LH2.^{17–19}

Among the key characteristics of natural light harvesting supramolecular chromophore assemblies, two are addressed in this study of synthetic nanorings. First is the role of static disorder, which shifts chromophore site energies, thus funnelling the electronic excitation energy toward the reaction centre.^{18,20–22} Second is the nontrivial coupling between electronic and nuclear degrees of freedom,^{23–26} possibly boosting excitation energy transfer efficiency^{23,27–29} and giving rise to “quantum beats” in their sub-ps domain transient spectra due to coherent nuclear motion in the ground and excited electronic states.^{30,31}

In studies of “quantum beating” phenomena it can be difficult to separate the features of ground and excited state vibrational wavepackets observed in fs transient absorption (fsTA). This is especially true in systems with small Huang-Rhys factors, such as chlorophylls,³² where partial overlap of the ground state bleach (GSB) and stimulated emission (SE) occurs, intertwining signatures of ground and excited state vibrational coherences.^{33,34} This picture can be further complicated by nonresonant contributions from solvent Raman active modes.^{31,35} Multidimensional spectroscopic techniques (in which information is spread over two, or more, frequency dimensions)^{33,36–39} provide a rigorous means of discriminating between ground and excited state vibrational coherences, but at the price of a more challenging experimental implementation and longer acquisition times. A feature which helps to differentiate between ground and excited state vibrations in conventional (one-dimensional) fs transient spectroscopies is the amplitude dip (or “node”) appearing at probe wavelengths corresponding to the maxima of the steady-state electronic absorption (for ground state nuclear wavepackets) or fluorescence (for excited state nuclear wavepackets) spectra. At these spectral positions, an abrupt π phase jump (“phase-flip”) of the oscillations occurs. Out-of-phase interference causes the amplitude of the oscillations to cancel at these wavelengths. Such a phenomenon has been previously described in the framework of a wavepacket evolving over time on a potential energy surface within a displaced harmonic oscillator model.^{33,37,40–42}

The impact of static disorder (inhomogeneous broadening) and coherently excited nuclear motion on exciton dynamics has been extensively investigated and modelled in the natural light-harvesting complexes.^{43–47} Less attention has been dedicated to investigating how such factors affect the photophysical behaviour of their man-made counterparts.^{19,48–50} Here we investigate the fs-to-ns population and sub-ps coherent dynamics of porphyrin nanorings, with size ranging from 10 to 40

chromophore units, by means of visible fs transient absorption with tuneable broadband excitation. The central wavelength of the pump pulses is tuned to be in resonance with either the blue or the red edges of the nanoring's steady-state absorption spectra. This reveals an excitation energy-dependent spectral profile and (coherent) dynamical behaviour in porphyrin nanorings. Such effects have previously been observed in inhomogeneously broadened ensembles such as linear conjugated oligomers and polymers^{34,51} and bacteriochlorophyll light-harvesting ring structures, but were not previously studied in size controlled conjugated nanorings.^{52,53}

Results and discussion

Steady-state electronic absorption and photoluminescence

The structure of the cyclic conjugated porphyrin nanorings is shown in the inset of Fig. 1. (Ar = 3,5-bis(octyloxy)phenyl). Normalised absorption and photoluminescence (PL) spectra are shown in Fig. 1. Steady-state electronic absorption and PL data in toluene with 1% pyridine have been previously reported and discussed,^{11,13} and are reproduced here to allow comparison to the NOPA pump pulses centred at either 720 nm (shaded blue area) or 860 nm (shaded red area).

Briefly, in large conjugated porphyrin nanorings, the HOMO-LUMO energy gap is inversely proportional to the number of repeating units (n_{por} , chromophores) over which the excitation is delocalised. This explains the redshift of the absorption spectra accompanying the increase in ring size from *c*-P10 to *c*-P30. No redshift is observed between *c*-P30 and *c*-P40 because the delocalisation length saturates at around 20 porphyrin units.^{11,13} The spectral bandwidth of large nanorings is a trade-off between exchange narrowing, yielding a narrower bandwidth for longer conjugation lengths, and line broadening effects arising from structural disorder, which is greater for larger rings. The combination of these two effects produces the observed narrowing from *c*-P10 to *c*-P30 followed by a slight broadening in the spectrum of *c*-P40.¹¹

The asymmetrical and broad spectra (Fig. 1) suggest static disorder in the ground state of large porphyrin nanorings, arising from a wide distribution of torsional angles between neighbouring porphyrins.^{10,54} As the angle between adjacent porphyrins affects both the exciton delocalisation length and the transition dipole moment,⁵⁴ the oscillator strength of different subsets of the broadened ground state population can differ significantly. At every wavelength, the optical density is proportional to both the average number of molecules $\langle n \rangle$ and the square modulus of the transition dipole moment $|\mu|^2$. Therefore, we can suggest that the high-energy side of the steady-state absorption spectrum arises from nanorings with a more "twisted" conformation along the butadiyne axis. These will display a weak transition dipole moment and shorter conjugation length. On the other hand, the low-energy side of the absorption spectrum is assigned to a population of nanorings whose torsional angles are small, thus allowing for more extended delocalisation length and stronger transition dipole moments. This assignment is in agreement with a previous experimental and theoretical study of a butadiyne linked Zn porphyrin dimer.⁵⁵

Normalised photoluminescence spectra of $c\text{-Pn}_{\text{por}}$ are shown as dashed lines in Fig. 1. The emission spectra of $c\text{-P20-40}$ are substantially overlapping, peaking at 860 nm, consistent with the similar nature of the excited states of $c\text{-P20-40}$, while the emission maximum of $c\text{-P10}$ is shifted to slightly lower energy (865 nm). The bandwidth of the photoluminescence spectra are narrower than the absorption spectra. This suggests that the emission comes from a narrower distribution of nanoring structures following excitation by (relatively) narrowband 750 nm excitation pulses (100 fs, 9 nm FWHM),¹³ suggesting some excited state evolution. Furthermore, all photoluminescence spectra have a peak at 970 nm (975 nm for $c\text{-P10}$). This feature is most likely vibronic in origin.

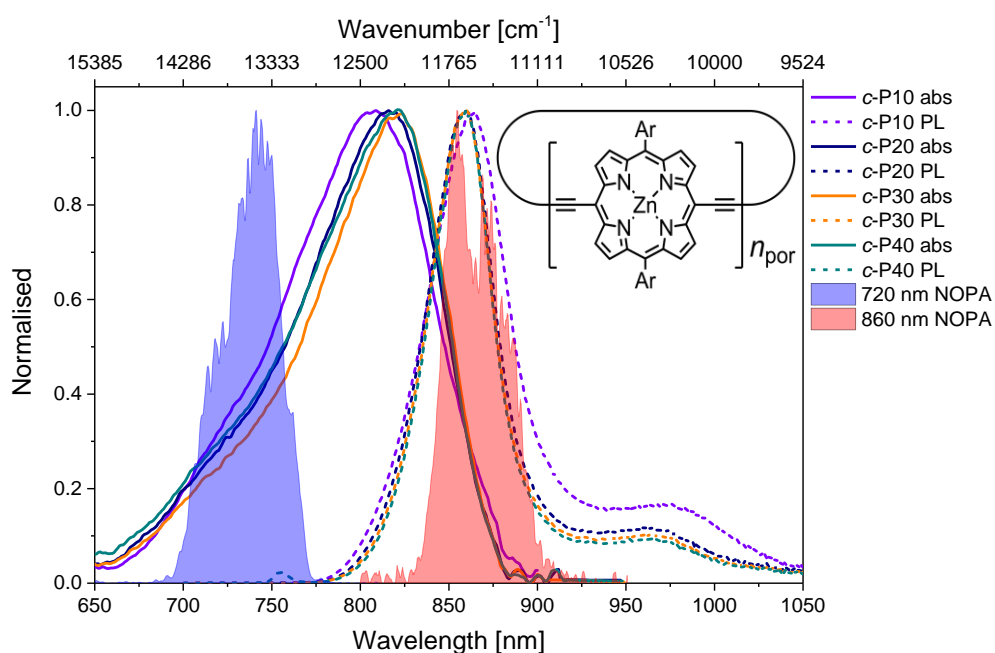


Fig. 1 Normalised steady-state absorption (solid lines) and photoluminescence (dashed lines, excitation at 750 nm) of $c\text{-P10}$ (violet) $c\text{-P20}$ (navy), $c\text{-P30}$ (orange) and $c\text{-P40}$ (teal). The normalised pump pulse spectra are shown as blue (720 nm) and red (860 nm) shaded areas. A sketch of the molecular structure of the cyclic conjugated porphyrin nanorings is shown in the inset. Ar = 3,5-bis(octyloxy)phenyl.

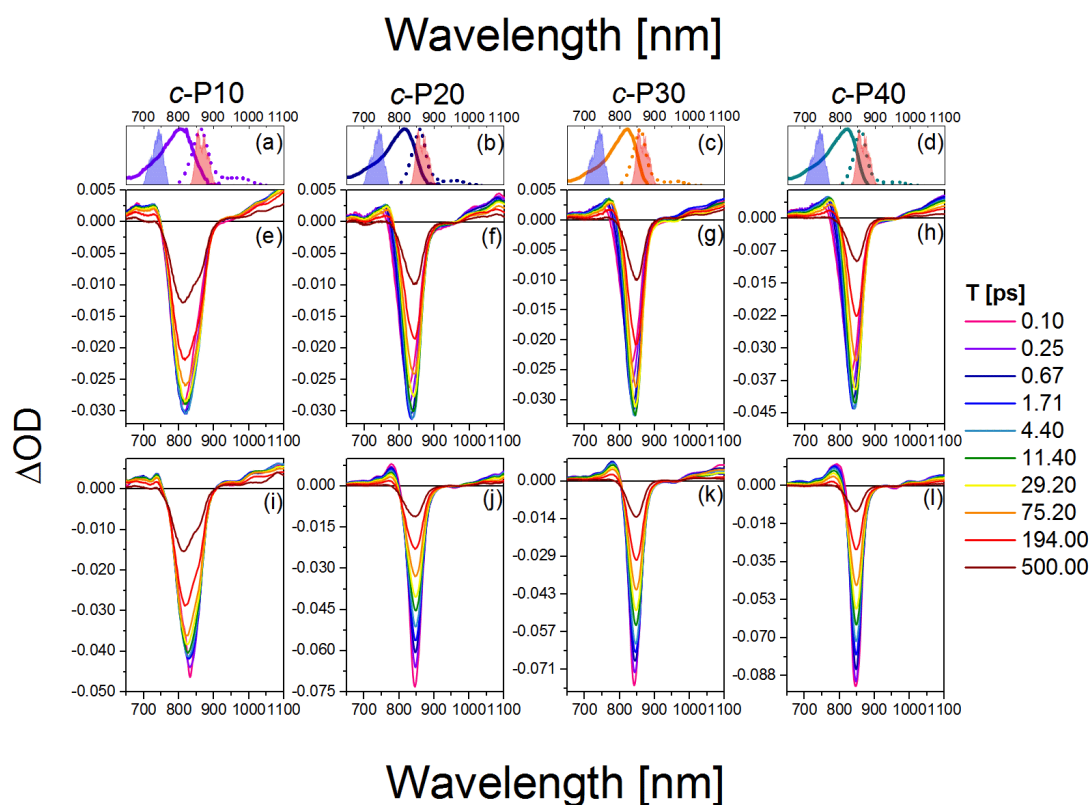


Fig. 2 fsTA data between 0.1 ps and 500 ps after excitation of c-P10 (e,i), c-P20 (f,j), c-P30 (g,k), and c-P40 (h,l) with 720 nm (e-h) or 860 nm (i-l) centred pump pulses. The pump spectra are shown as blue (720 nm) or red (860 nm) shaded areas in the top panels. Top panels (a-d) also report the steady state absorption and photoluminescence spectra of each nanoring as solid and dashed lines, respectively, following the colour code used in Figure 1.

The transient absorption spectra of c-Pn_{por} at ten, logarithmically spaced, pump-probe delay times (T) between 0.1 and 500 ps are shown in Fig. 2 e-h for excitation with 720 nm centred pump pulses and in Fig. 2 i-l for excitation with 860 nm centred pump pulses. To aid assignment, steady-state absorption (solid lines) and photoluminescence (dashed lines) of c-Pn_{por}, together with the spectra of the NOPA pulses (blue and red shaded areas) used for the two series of measurements, are shown in panels a-d.

The main feature of the transient absorption spectra of c-Pn_{por} after 720 nm excitation is a prominent negative band, present from the earliest times (as shown for $T = 0.1$ ps, solid magenta lines) with minima at 811 nm for c-P10, at 825 nm for c-P20, and at 830 nm for c-P30 and c-P40. These signals are slightly red-shifted with respect to the maxima of the steady-state absorption spectra of each nanoring. This red-shift reflects a contribution from prompt SE from the Franck-Condon state. Negative bands are thus assigned to a convolution of the bleaching of the ground state population

(GSB) and stimulated emission (SE). Unusually, these negative bands show an increase in amplitude (i.e. a deeper negative signal) as well as a redshift as a function of delay, T . This results in a noticeable band reshaping and redshift over the first 10 ps after photoexcitation, and the minima of the transient spectra at $T = 10$ ps appear at 820 nm for *c*-P10, and 845 nm for *c*-P20-40. The absolute amplitude growth of the region between 825 and 880 nm of the negative band is small for *c*-P10 but becomes more prominent as the size of the rings increases. The region of negative signal spectrally matches the wavelengths for which *c*-Pn_{por} photoluminescence is detected and is thus assigned to stimulated emission (SE) from a region of the excited state potential energy surface which is not promptly populated by 720 nm excitation. On longer timescales (10 to 100 ps), the negative minima of *c*-Pn_{por} are further shifting to the red in *c*-P20-40. The positive signals between 730 and 780 nm on the blue side of the negative bands are assigned to $S_1 \rightarrow S_n$ excited state absorption (ESA) contributions, whose risetime and redshift in the first 10 ps followed by slower, further shift to the red and relaxation to baseline in 500 ps in *c*-P20-40, match the dynamical evolution of the negative GSB + SE bands. A broad, weak and featureless ESA between 1000 and 1200 nm is present from the earliest measured pump-probe delay time. Its dynamics are remarkably different from the 760 nm ESA, as this NIR ESA displays non-monoexponential relaxation to baseline within 1 ns without any evidence of a risetime.¹¹

The dynamics retrieved upon excitation by 860 nm centred pump pulses (red shaded areas in Fig. 2 a-d) are strikingly different, as no fast increase in amplitude of the negative band, nor redshift are observed. The earliest time transient spectra ($T = 0.1$ ps) show an intense narrow negative feature peaked at 825 nm for *c*-P10 and 842 nm for *c*-P20-40. In sharp contrast to 720 nm excitation, these signals exhibit a 20% amplitude decrease within the first 1-2 ps, followed by slow redshift and non-monoexponential decay over tens to hundreds of ps. In *c*-P10 only, asymmetrical broadening towards the blue occurs over the same timescale, giving rise to a double minimum band, as observed (over the same timescale) in the data obtained for 720 nm excitation. The positive ESA signals, between 740 and 790 nm have maximum amplitude at $T = 0.1$ ps and experience multiexponential relaxation to baseline within 500 ps, without any significant spectral shifts. In both pumping conditions, the negative bands of *c*-Pn_{por} are not completely recovered even at the longest experimentally measured pump-probe delay time. The NIR ESA dynamics closely match those observed with 720 nm pump.

To highlight the dissimilar kinetics of the negative GSB+SE band in *c*-Pn_{por} after excitation at different wavelengths, a comparison of the time traces (probe wavelengths = 842 nm and 1100 nm) of *c*-P40 excited at 720 and 860 nm is reported, as an example, in Fig. S2. A comparison of the transient spectra of *c*-P40 excited at 720 or 860 nm for $T = 0.1, 4.5$ and 500 ps is shown in Fig. S3. Similar excitation wavelength dependent dynamics and spectral shapes were reported by Chang *et al.*⁵⁴ in a time-resolved photoluminescence study of a linear, butadiyne linked, porphyrin octamer.

Despite using the same pump pulse energy (10 nJ) at both the 720 and 860 nm, and the convolution between the normalised steady-state absorption and pump spectra being 15% larger for the 720 nm pump, the amplitude of the negative GSB+SE signals is much smaller when *c*-Pn_{por} are excited at 720 nm ($m\Delta OD = -30, -45$ at $T = 5$ ps) than at 860 nm ($m\Delta OD = -50, -90$ at $T = 0.1$ ps) (Fig. 2e-l). Such a

difference is in agreement with the assignment of transition dipole moment strength increasing toward the red side of the inhomogeneously broadened ground state nanoring population. The possibility of the difference in amplitude being due to a larger excited state population created by the 860 nm excitation is further ruled out by the behaviour of the broad ESA between 1050-1200 nm (ESA traces at 1100 nm shown in fig. S2). This signal does not show any appreciable amplitude variation as a function of the excitation wavelength (being specifically 6 m Δ OD for 720 nm pump, 5 m Δ OD for 860 nm pump at $T = 0.1$ ps).

To quantify the dynamical evolution of the fs transient absorption spectra, and highlight the different dynamical behaviour observed by tuning the pump wavelength, a global fitting analysis (using Glotaran)⁵⁶ was applied to all the datasets, assuming sequential evolution through a series of first-order steps. The resulting normalised evolution-associated difference spectra (EADS) are reported in Fig. 3. Due to the similarities in their transient photophysical behaviour, the EADS of *c*-P20-40 are discussed together.

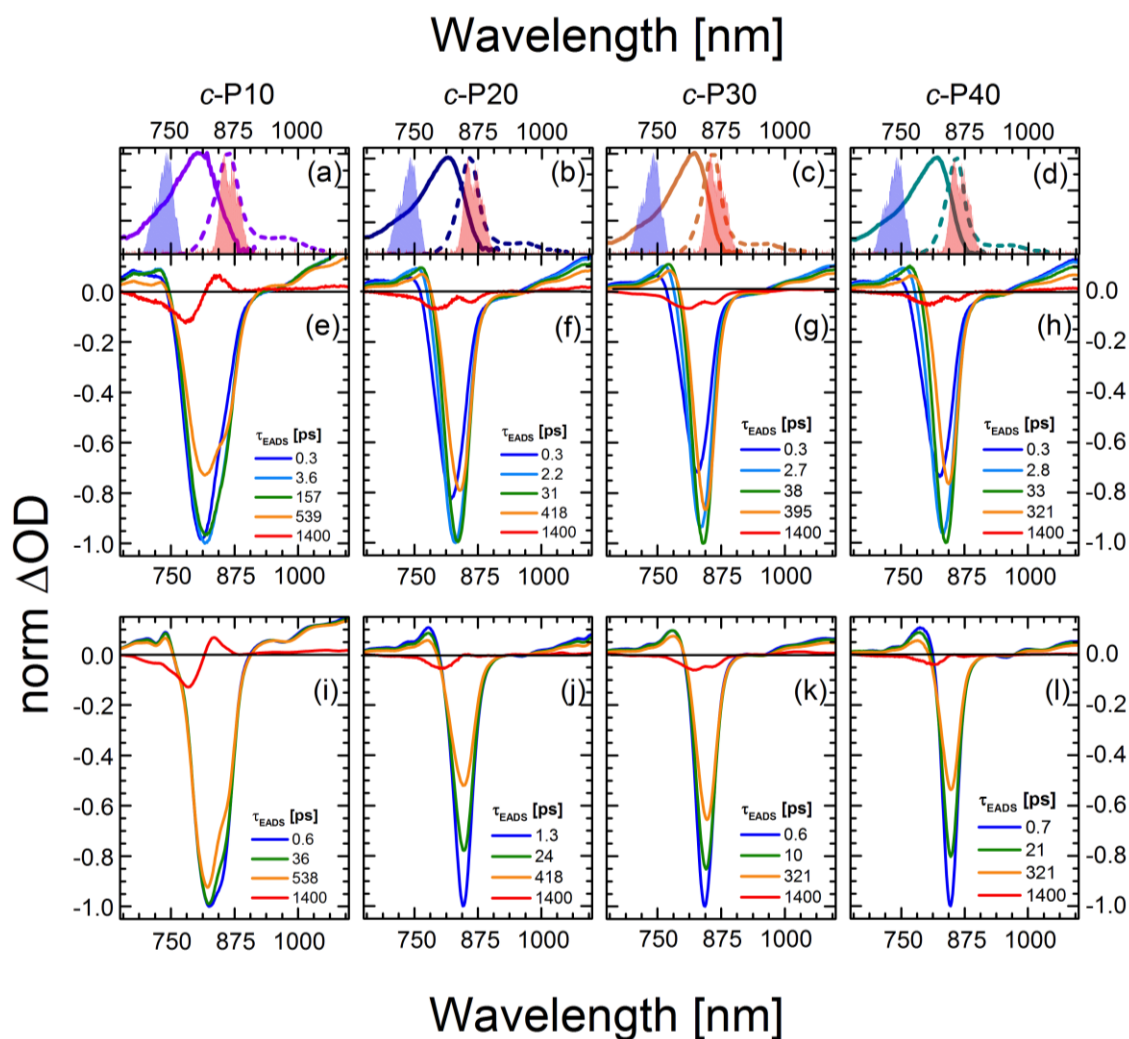


Fig. 3 Normalised evolution associated difference spectra (EADS) obtained by global fitting of the fsTA data of *c*-P10 (e,i), *c*-P20 (f,j), *c*-P30 (g,k), and *c*-P40 (h,l) after excitation with 720 nm (e-h) or 860 nm (i-l) centred pump pulses. The pump spectra

are shown as blue (720 nm) or red (860 nm) shaded areas in the top panels. Top panels (a-d) also report the steady state absorption and photoluminescence spectra of each nanoring as solid and dashed lines, respectively, following the colour code used in Figure 1.

Five components were necessary to obtain good fits to the experimental data of $c\text{-Pn}_{\text{por}}$ excited at 720 nm. The fastest components (0.3 ps, dark blue solid lines in Fig. 3 e-h and 2.2 – 2.8 in $c\text{-P20-40}$, light blue solid lines in Fig. 3 f-h) account for the redshift and a 20-25% relative amplitude increase of the negative band. We assign this deeper red-shifting negative signal to development of a more intense stimulated emission signal, as a function of time after photoexcitation on the blue side of the steady-state absorption of $c\text{-P20-40}$. The positive excited state absorption signals around 750 nm display the same red-shifting and rising behaviours, which are not reflected in the EADS region between 1050 and 1200 nm. Such SE and ESA rise times and redshifts may arise from non-single exponential relaxation of the initial exciton toward a region of the excited state PES with increased transition dipole moment along an inhomogeneously broadened distribution of structures. Similar phenomena have been observed for singlet excitations of highly conjugated organic oligomers and polymers.^{57,58} Additional evidence for inhomogeneity in $c\text{-Pn}_{\text{por}}$ is given by the linewidth of the emission spectra (dashed lines in panels a-d of Fig. 3) obtained upon narrowband excitation (~ 9 nm FWHM) at 750 nm.¹³ The emission spectra are substantially narrower than the corresponding absorption features (solid lines in panels a-d of Fig. 3).

A smaller red-shift and amplitude increase of the negative band is observed on a comparable timescale in $c\text{-P10}$, which lies in the transition regime between the behaviour of the fully delocalised nanoring $c\text{-P6}$, which does not show a delayed formation of the SE band when excited on the blue edge of its steady-state absorption spectrum,¹⁰ and the large $c\text{-P20-40}$ rings, whose exciton coherence lengths do not span their whole ring circumference.

On longer timescales, the 31-38 ps components measured in $c\text{-P20-40}$ (dark green solid lines in fig. 3 f-h) reflect a further redshift of the SE and of the 760 nm centred ESA band. The risetime and redshift of this ESA signal match the evolution of the GSB+SE negative signal occurring over the same timescale. The same EADS accounts for a 20% amplitude reduction of the negative signal. These components are assigned to structural dynamics involving the planarisation of the dihedral angle between neighbouring porphyrin units in the rings. Analogous structural dynamics have been observed, on a slower timescale (200 ps), for a six-membered porphyrin ring of the same family^{10,59} We speculate here that the planarisation rate is directly proportional to the ring circumference, as larger rings present more flexible structures and reduced strain. Such a speculation is supported by the fact that the planarization in $c\text{-P10}$ excited at 720 nm (solid dark green line in Fig. 3 e) has a time constant of ca. 160 ps, in-between the values measured for $c\text{-P6}$ and $c\text{-P20-40}$. The second longest component (solid orange lines in fig. 3 e-h) with time constants in the region of 300 to 600 ps, account for an overall decay of the transient spectra due to population relaxation back to the ground state, while the minor long-lived components (solid red lines in fig. 3 e-h) are assigned to the incomplete recovery of the ground state due to some population being trapped in a long lived triplet state (whose lifetime cannot be experimentally resolved by our experiment) as a consequence of intersystem

crossing (ISC). Similar behaviour was previously observed with fsTA and cryogenic temperature transient EPR spectroscopies, in smaller porphyrin nanorings.^{10,60}

The data obtained upon excitation of *c*-Pn_{por} with 860 nm centred pump pulses required four time components to be properly fit, one less than in the 720 nm pump case. The fastest (0.6-1.3 ps), and most intense EADS component (solid dark blue lines in fig.3 i-l) are narrower and red-shifted compared to the earliest EADS obtained when the same molecules are excited by 720 nm centred pump pulses, reflecting the inhomogeneity in the ground state population. In fact, the fastest evolution-associated difference spectra measured after 860 nm excitation match the EADSs observed a few ps after 720 nm pumping (solid dark green lines in Fig. 3 e-h). Such an observation suggests that, when *c*-Pn_{por} are excited with pump pulses resonant with the red edge of their absorption spectrum, the low-energy, strongly emissive, sites within the inhomogeneous distribution are directly populated, giving rise to prompt, intense, stimulated emission signals centred at 850-854 nm.

The rapid relaxation of this component is assigned to an energetically downhill relaxation toward the minimum of the excited state potential energy surface, with a transition dipole moment that is smaller compared to the, initially populated, Franck-Condon (FC) state. This is reflected in the ca. 20% decay of the SE amplitude on this timescale. Such a fast decay of the SE band could in principle indicate the presence of a rapid population decay back to the ground state on a ps timescale. However, the $S_1 \rightarrow S_n$ excited state absorption (ESA) at 1050-1200 nm does not display any such fast relaxation, as shown by the time traces in Fig. S2 and in a previous work on exciton-exciton annihilation dynamics.¹¹ We thus propose that the measured fast SE decay is due to relaxation of the, vertically excited, FC state to a region of the excited state PES with decreased transition dipole moment rather than to a population relaxation.

On longer timescales, the EADS of *c*-Pn_{por} present a minimal red-shift of 3-4 nm and undergo non-monoexponential decay assigned to S_1 population relaxation, with components in the tens (planarisation) and hundreds (S_1 population decay) of ps range, closely resembling the dynamics observed upon 720 nm excitation over the same timescale, leading to nearly complete recovery of the ground state population on the ns timescale. The small residual, long-lived, GSB is again assigned to ISC. The weak positive signal centred at 815 nm in the longest EADS of *c*-P10, for both the 720 and 860 nm excitation conditions is therefore assigned to triplet-triplet ($T_1 \rightarrow T_n$) excited state absorption.

Tuning the pump wavelength across the steady-state absorption profile of *c*-Pn_{por} translates to remarkable differences in the early time transient spectra, consistent with an inhomogeneously broadened ensemble with a range of radiative transition moments and $S_0 \rightarrow S_1$ energies as a function of the torsional angle.⁵² Similar observations were described by Peeks *et al.* for the butadiyne linked, Zn porphyrin dimer.⁵⁵

A schematic level diagram representing ground and excited states potential energy surfaces involved in the early time dynamics of *c*-Pn_{por} excited at 720 and 860 nm is shown in Fig. 4. In this picture ground and excited states have different minima for the broad inhomogeneous structure distribution, most

probably in the torsion coordinate.^{10,55,59} Further, the transition dipole moment (TDM) is a function of the same coordinate. Excitation on the blue side of the inhomogeneous ground state population initially populates excited states with low TDM. This population evolves on a few picosecond timescale towards the excited state minimum, which has a larger TDM. On red edge excitation the initial population has a large TDM, and also relaxes on the picosecond timescale to attain the minimum on the excited state surface, now with a reduced TDM compared to the initial state populated. This model is consistent with experimental observations of the wavelength dependent SE, although the non-single exponential nature of the relaxation dynamics may suggest more than one coordinate is involved in the excited state structural relaxation.

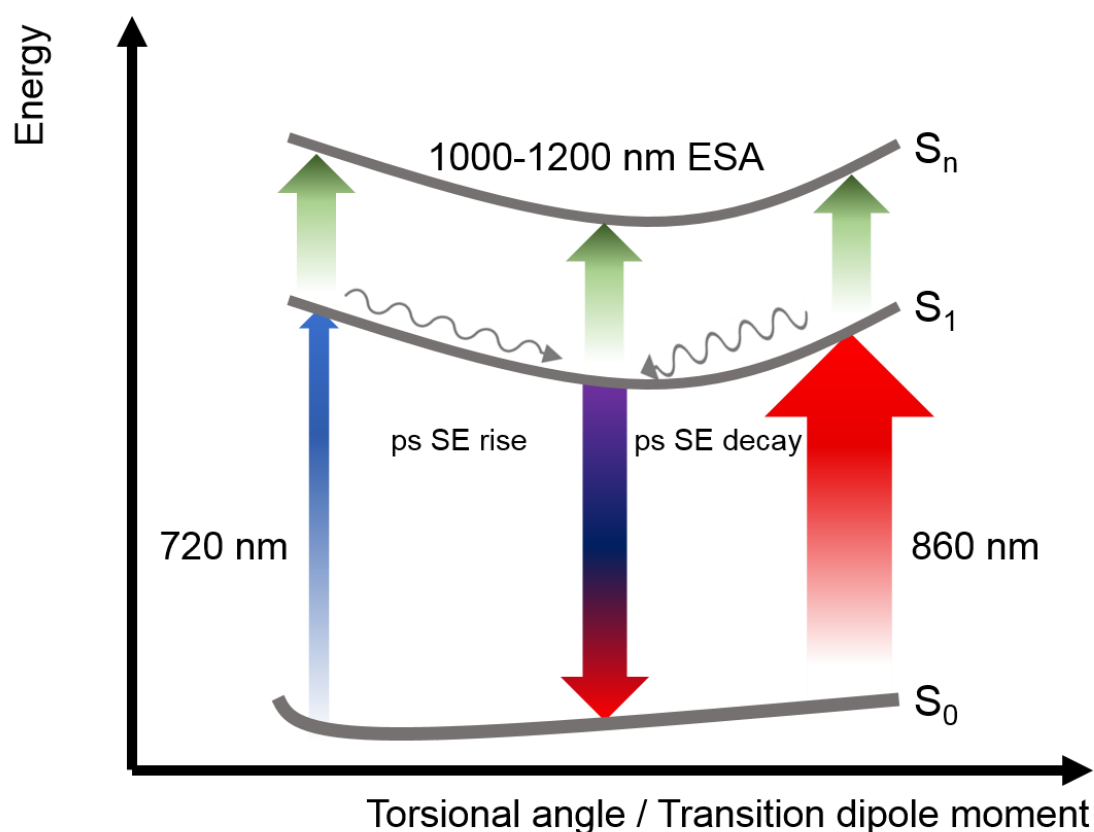


Fig. 4 Level diagram representing ground and excited states and fast dynamics of $c\text{-Pn}_{\text{por}}$. Transitions observed via fsTA after excitation with ultrashort 720 nm (blue upward arrow) or 860 nm (red upward arrow) pump pulses. Stimulated emission from the minimum of the excited state potential energy surface is represented as a blue/red downward arrow. $S_1 \rightarrow S_n$ NIR excited state absorption is represented as green upward arrows. The arrows thickness is proportional to the transition dipole moment of each transition. Relaxations in the excited state potential energy surface are represented by wavy arrows. Assignments are reported as well.

To obtain a clearer picture of how such differences in the excited state dynamics affect the coherent coupling of vibrational modes to the electronic transitions, we analysed the femtosecond coherence spectra (FCS) of $c\text{-Pn}_{\text{por}}$.

Coherent vibrational dynamics: fs coherence spectroscopy

Removing the relaxation dynamics by subtracting the multiexponential global fits (shown in Fig. 3) to the population dynamics from the fsTA data of $c\text{-Pn}_{\text{por}}$ (shown in Fig. 2) permits isolation of their sub-ps coherent behaviour, which arises from the generation and evolution of ground and excited state vibrational wavepackets.^{37,40}

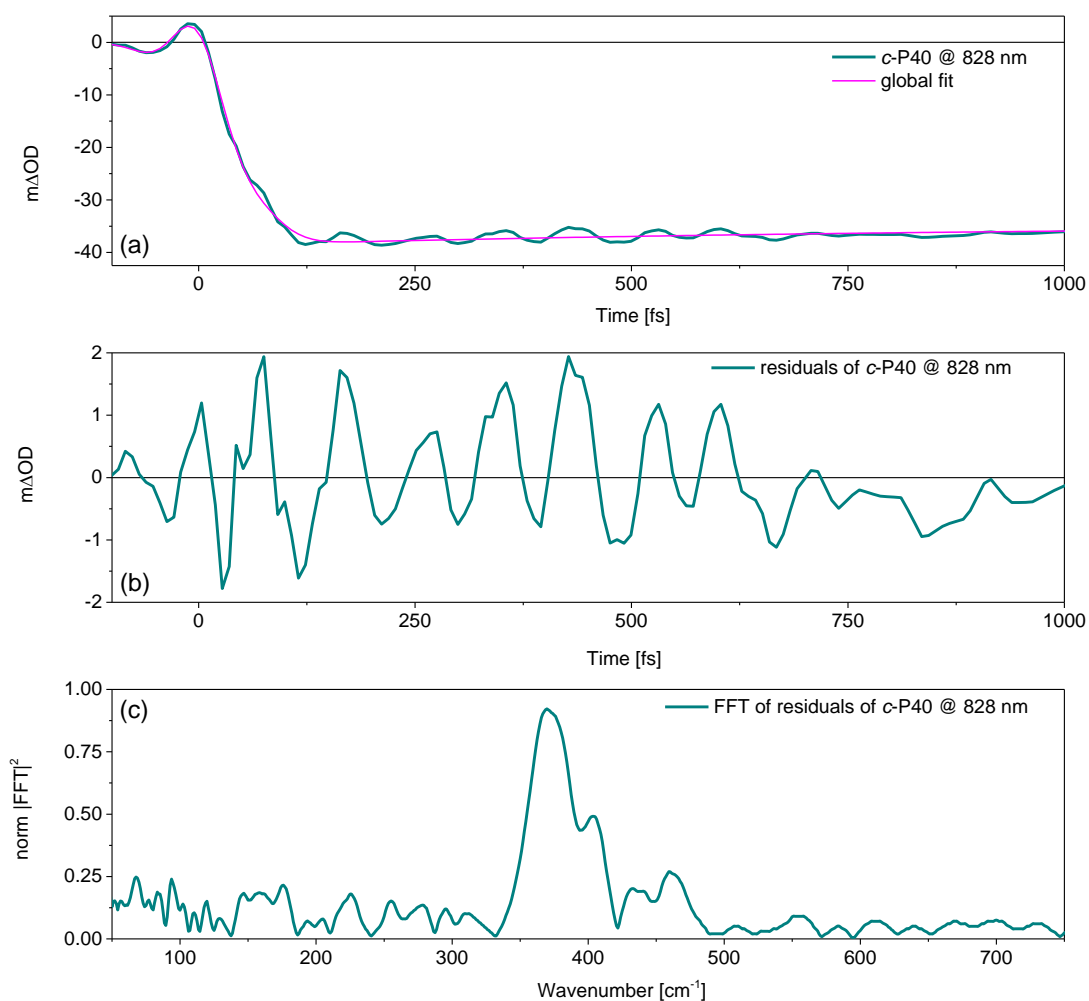


Fig. 5 a: Transient response of $c\text{-P40}$ (solid teal line) pumped with NOPA pulses centred at 860 nm, measured at a probe wavelength of 828 nm, showing fast oscillatory and slower relaxation dynamics. A trace at 828 nm taken from the global fit of the data is overlaid as a solid magenta line. The contribution of the sub-ps decaying component is minor at this wavelength as this trace was taken toward the blue edge of the negative GSB+SE signal, where oscillation amplitude is maximised. b: fast oscillatory behaviour of $c\text{-P40}$ isolated by the subtraction of the global fit from the experimental data. Note the difference between the maxima and minima of the ordinate axes of (a) and (b). c: Fourier transform of the fast oscillations shown in 4b, displaying a dominant resonance Raman mode at 370 cm^{-1} .

Fig. 5a shows an example of the behaviour of the transient oscillatory and slowly decaying response (for probe wavelength = 828 nm) obtained by pumping $c\text{-P40}$ with 860 nm centred NOPA pulses, overlaid with a trace from the global fit. The fast oscillatory response of $c\text{-P40}$, isolated by subtraction of the global fit is shown in Fig. 5b. The oscillatory behaviour has a ca. 85 fs period. The Fourier

transform of this oscillation is shown in Fig. 5c and displays a dominant mode at 370 cm^{-1} . Probe-wavelength resolved oscillatory behaviour is shown for c-P40 in Fig. 6a,b and for c-P10-30 in the Electronic Supplemental Information (Fig. S4)

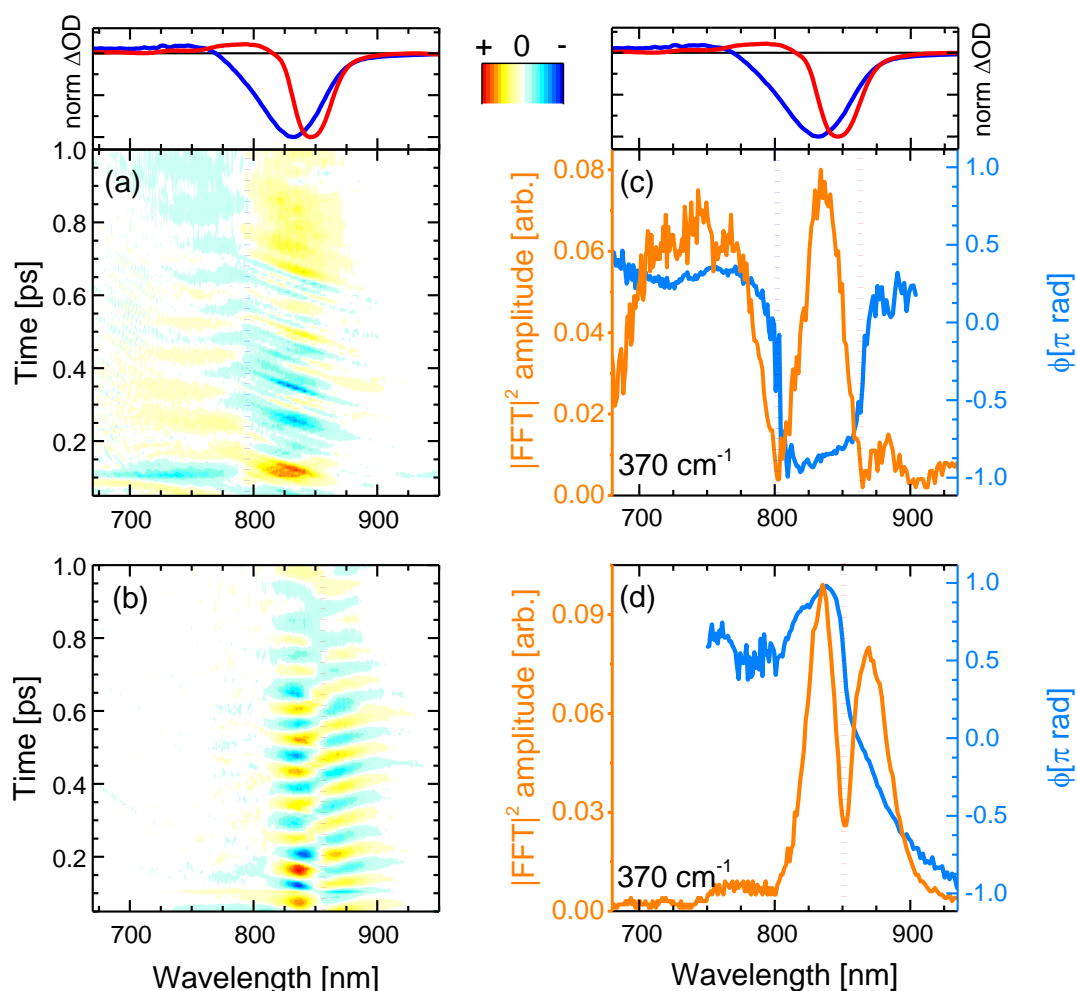


Fig. 6 a, b: Femtosecond Coherence Spectra of c-P40 after impulsive excitation by 720 or 860 nm broadband pump pulses. Numerical Fourier transformation of a, b yields phase and amplitude maps of the Raman active modes contributing to the time-domain beatings. c, d: probe wavelength-resolved amplitude (orange solid line) and phase (blue solid line) of the 370 cm^{-1} mode in the ground and excited electronic states of c-P40, respectively. Normalised fsTA spectra at $T = 100\text{ fs}$ of c-P40 excited at 720 and 860 nm are shown in the top panels as blue and red solid lines as a reference. Spectral positions at which the amplitude nodes/phase-flips occur for ground and excited state coherences are highlighted by vertical dotted blue and red lines, respectively. Oscillatory amplitude in panels a, b is normalized to the maximum and has 21 evenly-spaced contour lines.

When the pump pulses are centred at 720 nm, such beatings display an amplitude node (phase-flip) situated at 799 nm, which is on the blue side of both the steady-state absorption maximum (820 nm) and the fsTA GSB minimum ($T = 100\text{ fs}$, solid blue lines in top panels of Fig. 6), thus suggesting an assignment of these oscillations to a ground state vibrational coherence (c-P40 reported in Fig. 6a, c-

P10-30 in Fig. S4 d-f). The presence of the amplitude node to the blue of the steady-state absorption maximum (which all $c\text{-Pn}_{\text{por}}$ display when excited on the blue side of their steady-state absorption spectra, see Fig. S4d-f), is assigned to the inhomogeneous broadening (static disorder) in the ground state population of such large nanorings, as observed in the population dynamics discussed above. In the present case the 720 nm pump excites a blue shifted sub population. This observation indicates that the spectral diffusion in the ground state potential energy surface is slower than several picoseconds, such that the disorder experienced by the molecular ensembles is “frozen” over this timescale. The resulting broadening can thus be considered inhomogeneous on the timescales relevant for ground and excited state coherent nuclear wavepacket motion.

The static disorder permits selective excitation of a high-energy subset of nanorings within the inhomogeneous distribution by tuning the pump spectrum into resonance with the blue edge of the steady-state absorption spectra. Such a population experiences non-exponential fast motion toward a more allowed region of the excited state PES, with the fastest component relaxing with a time constant of 0.3 ps. We speculate that this fast relaxation promotes decoherence of the excited state vibrational wavepackets, as no oscillation with a node at a wavelength matching the photoluminescence maximum is observed in Fig. 6a. The time domain data only show a weak oscillation (600 $\mu\Delta\text{OD}$) with a node at 799 nm due to the ground state vibrational wavepacket contributions.⁶¹ The small amplitude of the ground state coherent vibrational oscillations may arise from broadband pulses bleaching to the same extent a wide distribution of ground state nuclear vibrational coordinates (distinct from the, lower energy, torsional coordinate causing the inhomogeneity), thus hampering the generation of a net ground state moving “hole”.^{37,61–64}

Numerical Fourier transformation of the time-domain data allowed retrieval of amplitude and phase of the 370 cm^{-1} mode as a function of the probe wavelength. These are shown as orange and light blue solid lines, respectively, in Fig. 6c. The presence of an abrupt π phase-jump at 860 nm (near the photoluminescence maximum) and of a weak peak between 860 and 900 nm suggest that, despite the absence of clear time-domain oscillations in this spectral region (Fig. 6a), residual excited state vibrational wavepackets are contributing to the coherent response of $c\text{-P40}$ excited by the 720 nm centred broadband pump pulses. The FT amplitude and phase profiles of $c\text{-P10-30}$ excited with NOPA pulses centred at 720 nm, on the blue side of their steady-state absorption spectra, show the same behaviour and are reported in Fig. S5.

When $c\text{-Pn}_{\text{por}}$ are excited by pump pulses in resonance with the red side of their steady-state absorption, the resulting femtosecond coherence spectra ($c\text{-P40}$ reported in Fig. 6b, $c\text{-P10-30}$ in Fig. S4 g-i) display an oscillatory behaviour with ca. 85 fs period and a node at 852-854 nm, matching the minima of the intense negative features of the earliest fsTA spectra (100 fs, red lines in top panels of Fig. 6) and the photoluminescence maxima (dashed lines in Fig. 1). Such beatings modulate the amplitude of the SE as a function of the pump-probe delay time and are thus assigned to vibrational wavepackets evolving in a strongly allowed region of S_1 . In this case, the oscillatory part of the transient response is dominated by stronger (2-3 $\text{m}\Delta\text{OD}$) excited state vibrational coherence

contributions, as there is no GSB amplitude (solid red lines in top panels of Fig. 6) around 750 nm, in the spectral region where the oscillatory features and node/phase-jump due to ground state vibrational wavepackets would be expected to appear.

Fig. 6d contains the same information shown in Fig. 6c for the oscillations measured upon excitation with 860 nm pump pulses. Fig. 6d shows how the dip in the power spectra amplitude (orange line) is accompanied by a phase-jump (light blue line), appearing at a wavelength matching the photoluminescence maximum, in agreement with the time-domain data. Such an effect is also observed in the amplitude and phase profiles of *c*-P10-30 excited with NOPA pulses centred at 860 nm, on the red edge of their steady-state absorption (Fig. S5).

Thus, the oscillatory features in the FCS of *c*-Pn_{por} excited by ultrashort broadband pump pulses are explained in terms of generation and evolution of vibrational wavepackets on the ground and excited state potential energy surfaces. This assignment is based on the spectral position of the amplitude nodes at, or near, the maxima of steady-state absorption or photoluminescence, in the context of a large inhomogeneous broadening causing remarkably different excited state population evolution as a function of the excitation wavelength.

Ground and excited state impulsive resonance Raman spectra

Integration of the probe wavelength-resolved Fourier transform of the time-domain oscillations shown in Figs. S6 and S7 over a limited range of probe wavelengths (700-800 nm for Raman maps obtained by 720 nm excitation, 810-900 nm for Raman maps obtained by 720 nm excitation) followed by amplitude normalisation yields the impulsive resonance Raman spectra of the ground and excited states of *c*-Pn_{por} (Figs. 7a and b, respectively). An analogous procedure was adopted by Fitzpatrick *et al.* to obtain impulsive Raman spectra of the organic dye cresyl violet.³³

The main contribution to the ground state Raman spectra of *c*-P30, 40 (Fig. 7a) is from the 370 cm⁻¹ peak (blue-shifted by 5 cm⁻¹ in *c*-P10, 20). Such a peak has been previously observed in the ZnTPP monomer,⁶⁵ in which it is slightly blue-shifted, appearing at 380 cm⁻¹. This dominant mode was detected in (templated) *c*-P6 at 380 cm⁻¹ in a cryogenic temperature 2D electronic spectroscopy study of Butkus *et al.*¹⁵ This contribution is assigned to Zn-N bonds stretches in the porphyrin cores.⁶⁶ The increase in ring size from *n* = 10 to 40 leads to a redshift, suggesting a reduction in the Zn-N force constant from the value in the monomer and six-membered ring. We speculate that the asymmetrical lineshape of these vibrational bands reflects the static disorder in the ground state ensemble.

A lower intensity mode peaking at 428 cm⁻¹ is also observed. This signal can be assigned to a combination of stretching and in-plane bending of the pyrrolic and methinic C-C bonds, following the assignment of Atamian *et al.*⁶⁶ for the parent ZnTPP monomer, in which the same mode is observed at 440 cm⁻¹. Butkus *et al.* identified a similar mode at 440 cm⁻¹ in (templated) *c*-P6.¹⁵ Finally, in Fig 7a there is a solvent contribution from toluene Raman active modes between 525 and 900 cm⁻¹ which are well characterised in the literature at 530 (ν₁₃⁶⁷), 590, 650, 735 and 770 (ν₁₂⁶⁷), 830 cm⁻¹. These contributions are marked with asterisks in Fig. 7a and appear more intense in the normalised spectra

of smaller nanorings because the absolute amplitude of their ground state resonance Raman signals are weaker.

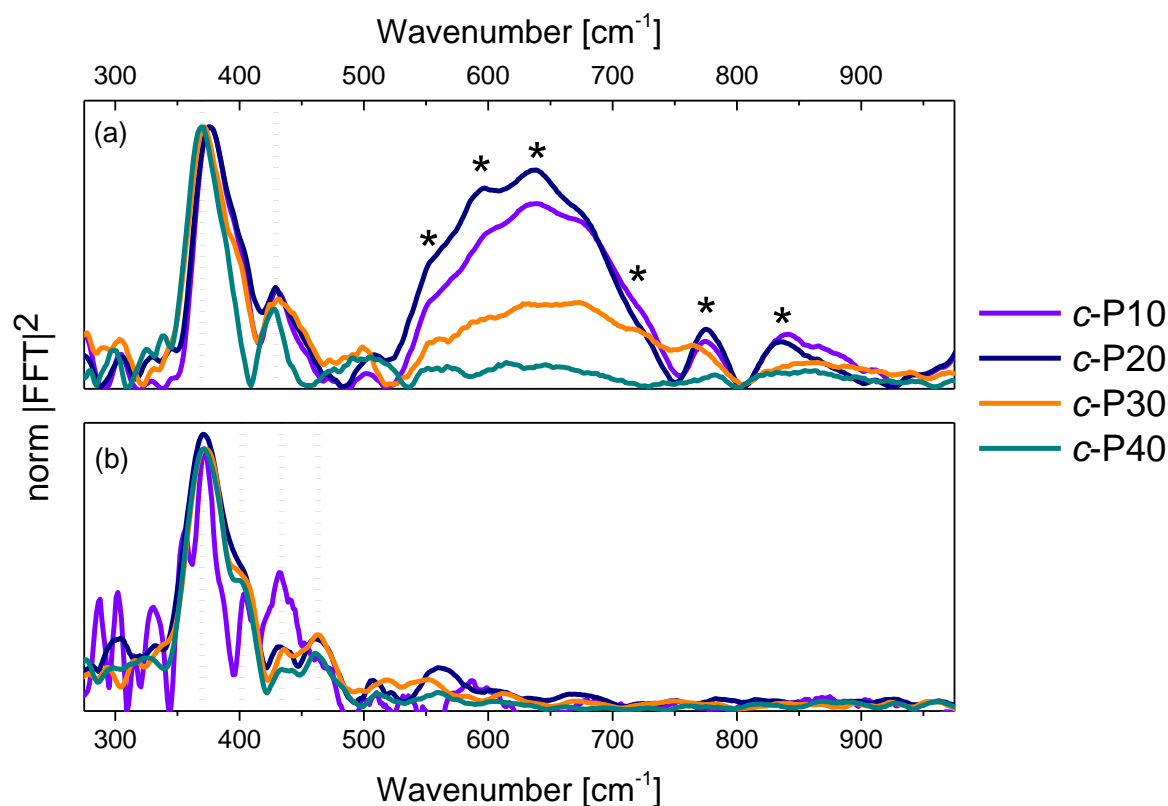


Fig. 7 Impulsive Raman spectra of *c*-P10 (violet), *c*-P20 (navy), *c*-P30 (orange) and *c*-P40 (teal) of their ground (a) and excited (b) electronic states. These spectra are obtained by integration of the Raman maps shown in Fig.4 over the probe wavelengths ranging from 720 to 850 nm (ground state Raman, a) or from 810 to 900 nm (excited state Raman, b). The asterisks indicate toluene (solvent) contributions to the impulsive ground state Raman spectra of *c*-P_{npor}. The signal-to-noise ratio of the ES impulsive resonance Raman spectrum of *c*-P10 (violet line in 6b) is low due to its small *f*sTA signal amplitude.

The excited state impulsive resonance Raman spectra of *c*-P20-40 (Fig. 7b) each display four signals, an intense peak at 370 cm⁻¹ with a well resolved shoulder at 402 cm⁻¹, and two weaker bands at 432 and 463 cm⁻¹. The 370 cm⁻¹ peaks were also observed in the corresponding GS impulsive Raman data and assigned to Zn-N stretching modes; these evidently do not display frequency shifts in the excited electronic states. This can be rationalised on the basis of the $\pi^* \leftarrow \pi$ nature of the underlying electronic transitions, whose charge density redistributions will only weakly influence molecular orbitals (MOs) involved in forming the Zn-N bonds.

We speculate that the shoulder centred at 402 cm⁻¹ could arise from a redshift of the stretching and in-plane bending of the pyrrolic and methinic C-C bonds mode with B_{1g} symmetry, observed at 428 cm⁻¹ in the GS resonance Raman. Zn porphyrin repeating unit of *c*-P_{npor} belong to the D_{2h} point group. In tetrapyrroles with D_{2h} symmetry, the B_{1g} MOs display bonding character between the pyrrolic

carbon nuclei displaced by the (B_{1g}) pyrrolic/methinic mode.^{66,68} Due to the bonding nature of the B_{1g} MO, the force constant of this vibrational mode is weakened in the S_1 excited state,⁶⁸ causing its redshift.

At higher wavenumbers, two weak peaks, centred at 433 and 462 cm^{-1} , contribute to the ES resonance Raman spectra of *c*-P20-40. No assignment is proposed for the 433 cm^{-1} mode, while the peak at 462 cm^{-1} is not observed in the GS of *c*-Pn_{por} and is assigned to a B_{1g} in-plane bending mode of the porphyrin backbone involving pyrrolic, methinic and phenylic (-Ar in the molecular structure shown in the inset of Fig. 2) nuclei.⁶⁶ The calculated ground state frequency for this mode is 490 cm^{-1} ,⁶⁶ but a redshift in the S_1 state is expected, as discussed above for the pyrrolic/methinic B_{1g} mode. The appearance of this mode in the ES spectra only of *c*-Pn_{por} is ascribed to a Raman scattering cross section enhancement of the methinic modes in the S_1 state, as a result of hyperconjugation between the tetrapyrrole π system with the $\sigma\pi$ MOs of the aryl side chains.⁶⁸

It is interesting to note that the sub-ps coherent dynamics observed in *c*-Pn_{por} are due to impulsive excitation of, ground and excited state, resonance Raman internal modes of the Zn porphyrin monomer. Such vibrations, localised on the monomeric unit, are coupled to transitions between delocalised electronic states whose exciton size spans several chromophores. Similar conclusions were reached by Dean *et al.*²⁷ who observed excited state vibrational coherences in light harvesting complexes, which were assigned to localised modes of constituent monomers. A recent polarisation-resolved 2D-ES study of the B850 complex also revealed that the vibrational modes coupled to its electronic transitions have monomeric (chlorophyll) character.⁵³

Conclusions

Population and coherent vibrational dynamics in fully-conjugated nanorings made up of 10 to 40, alkyne-bridged Zn-porphyrins were studied by femtosecond visible transient absorption spectroscopy using broadband pump pulses whose central wavelength was tuned to resonance with either the blue or red edges of the nanorings steady-state absorption spectra. The population dynamics obtained in the two different excitation conditions present striking differences due to inhomogeneous broadening. When the nanorings are excited at 720 nm, a non-single exponential relaxation in the excited state leads to a 10 nm redshift within the first picoseconds after photoexcitation, accompanied by the appearance of a more intense stimulated emission. These early-time dynamics are remarkably different to the data obtained upon excitation of the low-energy edge of the inhomogeneously broadened steady-state absorption at 860 nm. In that case the transient spectra present strong and prompt stimulated emission from a strongly allowed region of the S_1 potential energy surface, whose amplitude decays by 20% within the first couple of ps after photoexcitation populating a region of the excited state potential with lower transition dipole moment. The differences between the spectra obtained in the two excitation conditions vanish for longer pump-probe delay times, suggesting the excited state structural dynamics are complete. Such differences in the fast dynamics of porphyrin nanorings are thus assigned to variation of transition dipole moments across the inhomogeneously

broadened population. The observed dynamics are consistent with displaced minima and different curvatures for the ground and excited state potential energy surfaces along the torsional coordinate.

Coherent vibrational wavepacket dynamics, observed as modulations of the signal amplitude with an 85 fs period, display amplitude nodes (π phase-jumps) in spectral regions corresponding to the steady-state absorption or photoluminescence. This permits assignment of such oscillations to wavepackets evolving on either the ground or excited electronic states.

Impulsive Raman spectra of the ground and the excited state of each nanoring were obtained. The impulsive ground and excited state resonance Raman spectra between the series of *c*-Pn_{por} nanorings are very similar. This is in contrast to their radically different excitonic structures. This result allows us to conclude that in this class of macromolecules the nuclear wavepackets are localised on the Zn porphyrin repeating units and are only weakly influenced by the degree of electronic delocalisation.

The largest contribution to both the ground and the excited state low-frequency resonance Raman spectra of *c*-Pn_{por} is a 370 cm⁻¹ Zn-N stretching mode, previously observed at slightly higher frequency in a Zn porphyrin parent monomer. The second most intense peak, observed at 428 cm⁻¹ in the ground states, is assigned to a stretching and in-plane bending mode of the methinic and pyrrolic C-C bonds. We speculate that such a mode is redshifted by 26 cm⁻¹ in the excited electronic states due to alterations in the bonding character of the B_{1g} molecular orbitals upon electronic excitation of tetrapyrroles belonging to the D_{2h} point group.

Data Availability

The data that support the findings of this contribution are available from the corresponding authors upon reasonable request.

Conflicts of Interest

The authors declare no competing financial interest.

Acknowledgments

G.B., I.A.H. and S.R.M. acknowledge support from the Engineering and Physical Sciences Research Council under Awards No. EP/J009148/1, EP/J007161/1 and J021431/1. H.L.A. acknowledges support from the ERC (grant 320969) and EPSRC (EP/M016110/1). M.J. thanks Oxford University for a Scatcherd European Scholarship. We would like to thank Dr Palas Roy and Dr Dale Green for the helpful discussions.

Notes and References

- 1 C. G. Claessens, D. González-Rodríguez, M. S. Rodríguez-Morgade, A. Medina and T. Torres, *Chem. Rev.*, 2014, **114**, 2192–2277.
- 2 H. L. Anderson, *ChemInform*, 2010, **31**, 2323–2330.
- 3 P. Roy, G. Bressan, J. Gretton, A. N. Cammidge and S. R. Meech, *Angew. Chemie Int. Ed.*, 2021, **60**, 10568–10572.

- 4 G. Bressan, A. N. Cammidge, G. A. Jones, I. A. Heisler, D. Gonzalez-Lucas, S. Remiro-Buenamañana and S. R. Meech, *J. Phys. Chem. A*, 2019, **123**, 5724–5733.
- 5 J. Oh, Y. M. Sung, Y. Hong and D. Kim, *Acc. Chem. Res.*, 2018, **51**, 1349–1358.
- 6 H. Z. Yu, J. S. Baskin and A. H. Zewail, *J. Phys. Chem. A*, 2002, **106**, 9845–9854.
- 7 J. S. Baskin, H. Z. Yu and A. H. Zewail, *J. Phys. Chem. A*, 2002, **106**, 9837–9844.
- 8 L. Bolzonello, F. Fassioli and E. Collini, *J. Phys. Chem. Lett.*, 2016, **7**, 4996–5001.
- 9 D. V. Kondratuk, L. M. A. Perdigaõ, A. M. S. Esmail, J. N. O’Shea, P. H. Beton and H. L. Anderson, *Nat. Chem.*, 2015, **7**, 317–322.
- 10 G. Bressan, M. D. Peeks, H. L. Anderson, S. R. Meech and I. A. Heisler, *J. Phys. Chem. C*, 2019, **123**, 27222–27229.
- 11 G. Bressan, M. Jirasek, H. L. Anderson, I. A. Heisler and S. R. Meech, *J. Phys. Chem. C*, 2020, **124**, 18416–18425.
- 12 J. K. Sprafke, D. V. Kondratuk, M. Wykes, A. L. Thompson, M. Hoffmann, R. Drevinskas, W.-H. Chen, C. K. Yong, J. Kärnbratt, J. E. Bullock, M. Malfois, M. R. Wasielewski, B. Albinsson, L. M. Herz, D. Zigmantas, D. Beljonne and H. L. Anderson, *J. Am. Chem. Soc.*, 2011, **133**, 17262–17273.
- 13 P. Parkinson, D. V. Kondratuk, C. Menelaou, J. Q. Gong, H. L. Anderson and L. M. Herz, *J. Phys. Chem. Lett.*, 2014, **5**, 4356–4361.
- 14 J. Q. Gong, L. Favereau, H. L. Anderson and L. M. Herz, *J. Phys. Chem. Lett.*, 2016, **7**, 332–338.
- 15 V. Butkus, J. Alster, E. Bašinskaite, R. Augulis, P. Neuhaus, L. Valkunas, H. L. Anderson, D. Abramavicius and D. Zigmantas, *J. Phys. Chem. Lett.*, 2017, **8**, 2344–2349.
- 16 C. J. Judd, A. S. Nizovtsev, R. Plougmann, D. V. Kondratuk, H. L. Anderson, E. Besley and A. Saywell, *Phys. Rev. Lett.*, 2020, **125**, 206803.
- 17 D. Abramavicius, L. Valkunas and R. Van Grondelle, *Phys. Chem. Chem. Phys.*, 2004, **6**, 3097–3105.
- 18 R. J. Cogdell, A. Gall and J. Köhler, *Q. Rev. Biophys.*, 2006, **39**, 227–324.
- 19 C.-K. Yong, P. Parkinson, D. V. Kondratuk, W.-H. Chen, A. Stannard, A. Summerfield, J. K. Sprafke, M. C. O’Sullivan, P. H. Beton, H. L. Anderson and L. M. Herz, *Chem. Sci.*, 2015, **6**, 181–189.
- 20 H.-G. Duan, A. L. Stevens, P. Nalbach, M. Thorwart, V. I. Prokhorenko and R. J. Dwayne Miller, *J. Phys. Chem. B*, 2015, **119**, 12017–12027.
- 21 G. D. Scholes, *J. Phys. Chem. Lett.*, 2010, **1**, 2–8.
- 22 E. Fresch, E. Meneghin, A. Agostini, H. Paulsen, D. Carbonera and E. Collini, *J. Phys. Chem. Lett.*, 2020, **11**, 1059–1067.
- 23 D. M. Jonas, *Annu. Rev. Phys. Chem.*, 2018, **69**, 327–352.
- 24 H.-G. Duan, V. I. Prokhorenko, R. J. Cogdell, K. Ashraf, A. L. Stevens, M. Thorwart and R. J. D. Miller, *Proc. Natl. Acad. Sci.*, 2017, **114**, 8493–8498.
- 25 E. Thyryhaug, C. N. Lincoln, F. Branchi, G. Cerullo, V. Perlík, F. Šanda, H. Lokstein and J. Hauer, *Photosynth. Res.*, 2018, **135**, 45–54.

- 26 M. Maiuri, E. E. Ostroumov, R. G. Saer, R. E. Blankenship and G. D. Scholes, *Nat. Chem.*, 2018, **10**, 177–183.
- 27 J. C. Dean, T. Mirkovic, Z. S. D. Toa, D. G. Oblinsky and G. D. Scholes, *Chem*, 2016, **1**, 858–872.
- 28 A. Chenu, N. Christensson, H. F. Kauffmann and T. Mančal, *Sci. Rep.*, 2013, **3**, 2029.
- 29 H.-G. Duan, P. Nalbach, R. J. D. Miller and M. Thorwart, *Photosynth. Res.*, 2020, **144**, 137–145.
- 30 M. Liebel and P. Kukura, *J. Phys. Chem. Lett.*, 2013, **4**, 1358–1364.
- 31 M. Liebel, C. Schnedermann, T. Wende and P. Kukura, *J. Phys. Chem. A*, 2015, **119**, 9506–9517.
- 32 M. F. Gelin, L. Chen, R. Borrelli and E. Thyryhaug, *Chem. Phys.*, 2020, **528**, 110495.
- 33 C. Fitzpatrick, J. H. Othner and R. J. Levis, *J. Phys. Chem. A*, 2020, **124**, 6856–6866.
- 34 W. Barford and M. Marcus, *J. Chem. Phys.*, 2017, **146**, 130902.
- 35 Z. Zhang, A. Huerta-Viga and H.-S. Tan, *Opt. Lett.*, 2018, **43**, 939.
- 36 F. V. de A. Camargo, L. Grimmelsmann, H. L. Anderson, S. R. Meech and I. A. Heisler, *Phys. Rev. Lett.*, 2017, **118**, 033001.
- 37 P. C. Arpin and D. B. Turner, *J. Phys. Chem. A*, 2021, **125**, 2425–2435.
- 38 G. Bressan, D. Green, Y. Chan, P. C. Bulman Page, G. A. Jones, S. R. Meech and I. A. Heisler, *J. Phys. Chem. A*, 2019, **123**, 1594–1601.
- 39 G. Bressan and J. J. van Thor, *J. Chem. Phys.*, 2021, **154**, 244111.
- 40 D. B. Turner and P. C. Arpin, *Chem. Phys.*, 2020, **539**, 110948.
- 41 S. Rafiq and G. D. Scholes, *J. Phys. Chem. A*, 2016, **120**, 6792–6799.
- 42 G. Lee, J. Kim, S. Y. Kim, D. E. Kim and T. Joo, *ChemPhysChem*, 2017, **18**, 670–676.
- 43 K. J. Karki, J. Chen, A. Sakurai, Q. Shi, A. T. Gardiner, O. Kühn, R. J. Cogdell and T. Pullerits, *Chem. Sci.*, 2019, **10**, 7923–7928.
- 44 N. H. C. Lewis, N. L. Gruenke, T. A. A. Oliver, M. Ballottari, R. Bassi and G. R. Fleming, *J. Phys. Chem. Lett.*, 2016, **7**, 4197–4206.
- 45 G. Trinkunas, J. L. Herek, T. Polívka, V. Sundström and T. Pullerits, *Phys. Rev. Lett.*, 2001, **86**, 4167–4170.
- 46 Y. Yoneda, T. Noji, T. Katayama, N. Mizutani, D. Komori, M. Nango, H. Miyasaka, S. Itoh, Y. Nagasawa and T. Dewa, *J. Am. Chem. Soc.*, 2015, **137**, 13121–13129.
- 47 M. Ferretti, R. Hendrikx, E. Romero, J. Southall, R. J. Cogdell, V. I. Novoderezhkin, G. D. Scholes and R. van Grondelle, *Sci. Rep.*, 2016, **6**, 20834.
- 48 J. E. Donehue, O. P. Varnavski, R. Cemborski, M. Iyoda and T. Goodson, *J. Am. Chem. Soc.*, 2011, **133**, 4819–4828.
- 49 Y. Li, S. S. Rajasree, G. Y. Lee, J. Yu, J.-H. Tang, R. Ni, G. Li, K. N. Houk, P. Deria and P. J. Stang, *J. Am. Chem. Soc.*, 2021, **143**, 2908–2919.
- 50 W. J. Kendrick, M. Jirásek, M. D. Peeks, G. M. Greetham, I. V. Sazanovich, P. M. Donaldson, M. Towrie, A. W. Parker and H. L. Anderson, *Chem. Sci.*, 2020, **11**, 2112–2120.

- 51 M. Marcus, J. Coonjobeeharry and W. Barford, *J. Chem. Phys.*, , DOI:10.1063/1.4946794.
- 52 N. R. S. Reddy, G. J. Small, M. Seibert and R. Picorel, *Chem. Phys. Lett.*, 1991, **181**, 391–399.
- 53 J. Kim, T. C. Nguyen-Phan, A. T. Gardiner, T. H. Yoon, R. J. Cogdell, M. Cho and G. D. Scholes, *J. Phys. Chem. Lett.*, 2022, 1099–1106.
- 54 M.-H. Chang, M. Hoffmann, H. L. Anderson and L. M. Herz, *J. Am. Chem. Soc.*, 2008, **130**, 10171–10178.
- 55 M. D. Peeks, P. Neuhaus and H. L. Anderson, *Phys. Chem. Chem. Phys.*, 2016, **18**, 5264–5274.
- 56 J. J. Snellenburg, S. P. Laptенок, R. Seger, K. M. Mullen and I. H. M. van Stokkum, *J. Stat. Softw.*, 2012, **49**, 1–22.
- 57 S. T. Hoffmann, H. Bässler and A. Köhler, *J. Phys. Chem. B*, 2010, **114**, 17037–17048.
- 58 Y. V. Romanovskii and H. Bässler, *J. Lumin.*, 2005, **113**, 156–160.
- 59 F. V. A. Camargo, H. L. Anderson, S. R. Meech and I. A. Heisler, *J. Phys. Chem. B*, 2015, **119**, 14660–14667.
- 60 C. E. Tait, P. Neuhaus, M. D. Peeks, H. L. Anderson and C. R. Timmel, *J. Am. Chem. Soc.*, 2015, **137**, 8284–8293.
- 61 A. T. N. Kumar, F. Rosca, A. Widom and P. M. Champion, *J. Chem. Phys.*, 2001, **114**, 6795–6815.
- 62 J. Brazard, L. A. Bizimana, T. Gellen, W. P. Carbery and D. B. Turner, *J. Phys. Chem. Lett.*, 2016, **7**, 14–19.
- 63 V. Tiwari, W. K. Peters and D. M. Jonas, *Proc. Natl. Acad. Sci.*, 2013, **110**, 1203–1208.
- 64 D. M. Jonas, S. E. Bradforth, S. A. Passino and G. R. Fleming, *J. Phys. Chem.*, 1995, **99**, 2594–2608.
- 65 F. V. A. Camargo, H. L. Anderson, S. R. Meech and I. A. Heisler, *J. Phys. Chem. A*, 2014, **119**, 95–101.
- 66 M. Atamian, R. J. Donohoe, J. S. Lindsey and D. F. Bocian, *J. Phys. Chem.*, 1989, **93**, 2236–2243.
- 67 T. H. S. Bican, H. W. Schrötter and V. M. Grošev, *J. Raman Spectrosc.*, 1995, **26**, 787–790.
- 68 S. Sato, K. Aoyagi, T. Haya and T. Kitagawa, *J. Phys. Chem.*, 1995, **99**, 7766–7775.